Electromagnetic FWI of 2-D Inhomogeneous Objects Straddling Multiple Planar Layers by Finite-Element Boundary Integral and Levenberg–Marquardt Methods

Jiawen Li, Zili Li, Ruidong Huang, and Feng Han, *Senior Member, IEEE*

Abstract— This article extends the existing finite-element boundary integral (FEBI) method to account for electromagnetic (EM) scattering and inverse scattering from both isotropic and anisotropic 2-D inhomogeneous objects straddling multiple planar layers. In the forward scattering computation, the inhomogeneous scatterers placed across several layers are enclosed by a 1-D smooth boundary within which the finite element method (FEM) is implemented to solve for the 2-D EM field distribution. The integral equation (IE) is formulated on the 1-D boundary to form the radiation boundary condition (RBC) to truncate the FEM domain. The 2-D layered-medium dyadic Green's functions (DGFs) used in the boundary IE to solve for the equivalent current and used in the scattering data equations to compute the scattered fields at the receiver array are evaluated for both the transverse electric (TE) and transverse magnetic (TM) modes. In the full-wave inversion (FWI) to reconstruct isotropic scatterer dielectric parameters in the TE mode and anisotropic scatterer dielectric parameters in the TM mode, we compute the first-order derivatives of the system mass matrix with respect to isotropic model parameters and the first-order derivatives of the system stiffness matrix with respect to anisotropic model parameters to assemble the sensitivity matrices for the TE mode and TM mode, respectively. Finally, the Levenberg–Marquardt (LM) method is used to iteratively call the FEBI forward solver to fulfill the reconstruction. Numerical experiments are carried out to show the computation efficiency and correctness of the forward scattering and FWI solvers.

Index Terms— Electromagnetic (EM) scattering, finite-element boundary integral (FEBI) method, full-wave inversion (FWI), Levenberg–Marquardt (LM) method.

I. INTRODUCTION

ELECTROMAGNETIC (EM) full-wave inversion (FWI) aims at reconstructing the model parameters such as shapes, locations, sizes, and dielectric constants of the

Jiawen Li and Zili Li are with the School of Electronic and Information Engineering, Guangxi Normal University, Guilin, Guangxi 541004, China (e-mail: jiawenli@mailbox.gxnu.edu.cn; zlienishi@mailbox.gxnu.edu.cn).

Ruidong Huang is with the Institute of Electromagnetics and Acoustics and the Key Laboratory of Electromagnetic Wave Science and Detection Technology, Xiamen University, Xiamen 361005, China.

Feng Han is with the School of Computing and Information Technology, Great Bay University, Dongguan, Guangdong 523000, China, and also with the Institute of Electromagnetics and Acoustics, Xiamen University, Xiamen 361005, China (e-mail: feng.han@gbu.edu.cn; feng.han@xmu.edu.cn).

unknown targets from scattered EM fields recorded at the receiver array by strictly solving the scattering data equations [1]. Its wide applications include biomedical imaging [2], security screening [3], subsurface detection [4], deep Earth exploration [5], and so on.

Due to the intrinsic nonlinearity of the EM inversion problems, the traditional FWI methods usually need to iteratively call the forward scattering solvers and this iteration continues until the data misfits of the scattered fields become less than a prescribed threshold [6]. The most direct way to construct the forward solvers is by formulating the wave scattering process using the differential-form Maxwell equations or the Helmholtz equations, discretizing them, and finally solving them using some numerical methods. For example, the finite-difference time-domain (FDTD) method used to solve discrete Maxwell equations and proposed by Yee [7] has been applied to landmine detection by the ground penetrating radar (GPR) [8], to subsurface water content reconstruction from GPR data [9], to simulating 3-D transient EM (TEM) response from arbitrarily complicated distributions of Earth conductivity and magnetic permeability [10], and to the 3-D marine magnetotelluric (MT) data inversion [11]. On the other hand, the finite-difference frequency-domain (FDFD) method also has been applied to 3-D MT data inversion [12], to the interpretation of 3-D controlled-source EM (CSEM) data [13], and to 2.5-D logging-while-drilling (LWD) EM measurements [14]. Besides these finite difference methods, the finite element method (FEM) and the spectral element method (SEM) also have been widely adopted in EM FWI, especially in geophysical exploration. Typical applications include 3-D CSEM data inversion [15], 3-D MT data inversion with the local topography taken into account [16], computation of the surface-to-borehole EM (SBEM) system response [17], 3-D airborne EM (AEM) modeling [18], and CSEM hydrocarbon exploration [19]. Although these differential equation (DE)-based forward solvers have been successfully applied to EM FWI, especially for geophysical exploration in the low-frequency regime when the absorbing boundary condition (ABC) is imposed, their implementation efficiency is significantly lowered for the subsurface high-resolution reconstruction when the operation frequency is high and the transceivers are placed far from the inversion domain, e.g., for the air-launched GPR detection [20], since the regions

between the transceivers and the inversion domain also need to be discretized.

The integral equation (IE)-based forward solvers for EM FWI can avoid the redundant discretized regions because the transceivers and the inversion domain are linked by Green's functions. Due to the unaffordable computational cost of the original method of moment (MoM) [21], a series of fast algorithms have been proposed to solve the IE-based scattering problems, and their implementation efficiency is inspected in the FWI. The most commonly adopted approach is using the fast Fourier transform (FFT) to accelerate the integration of the multiplication of the equivalent current and Green's functions or to accelerate the multiplication of matrices and vectors. Representative methods include conjugate gradient FFT [22], biconjugate gradient (BCG) FFT [23], the stabilized BCG-FFT (BCGS-FFT) [24], the adaptive integral method (AIM) [25], and the precorrected-FFT (pFFT) method [26]. Most of these fast algorithms have been successfully applied to the EM FWI for crosswell measurements [27], multiparametric reconstruction of anisotropic objects embedded in multilayered media [28], and the reconstruction of high-contrast proppant [29]. Unfortunately, because the IE-based forward scattering solvers heavily depend on the availability of Green's functions, either via analytical derivation or numerical computation, the background medium must be regular enough, e.g., homogeneous, planarly layered, cylindrically layered, and spherically layered. Evaluation of Green's functions for arbitrarily inhomogeneous background used in an IE will incur massive extra computation costs [30]. In addition, even for a planarly layered background medium, placing the scatterers across multiple layers will lead to the disruption of the shift-invariance of Green's functions in the vertical direction and thus the failure of FFT acceleration [31], [32], [33], [34].

Therefore, in this article, we combine the FEM and Green's functions to efficiently solve the 2-D EM scattering and inverse scattering of inhomogeneous objects straddling multiple planar layers. The motivation for such a study is that the real subsurface medium is always stratified instead of homogeneous and the inhomogeneous anomalies are not necessarily concentrated inside one layer in the real EM detection [32]. The traditional IE-based methods are highly computational demanding for EM scattering in such a scenario [31], [32]. However, in our newly proposed hybrid scheme, the calculation can be accomplished without much additional costs for the computation domain traversing arbitrary planar layers and the transceivers placed far from it. The 2-D FEM is adopted to solve the discretized Helmholtz equation in the computation domain which is truncated by a radiation boundary condition (RBC). This RBC is formulated by the 1-D boundary IE and solved by the traditional MoM. Although this hybrid finite-element boundary integral (FEBI) method was proposed by pioneer researchers several decades ago [35] and has been adopted to solve 2-D and 3-D EM scattering problems previously [36], [37], [38], the background media are homogeneous and anisotropy materials are rarely considered in these works. Meanwhile, most previous works only dealt with the forward scattering problems. The inversion using the FEBI method was rarely treated. So, the major new contribution of this work is to extend the existing FEBI method to more complicated and practical EM scattering and inverse scattering applications. Specifically speaking, in the 2-D transverse electric (TE) mode, the inhomogeneous isotropic scatterers are allowed to straddle multiple subsurface isotropic planar layers. In the 2-D transverse magnetic (TM) mode, the inhomogeneous arbitrarily anisotropic scatterers are allowed to straddle multiple subsurface biaxially anisotropic planar layers. In the forward scattering computation, the FEBI is adopted to solve for the equivalent current on the 1-D boundary across multiple layers and the scattered fields at the receiver array. In the FWI, the sensitivity matrices are assembled for both the TE and TM modes in the framework of FEBI. The Levenberg–Marquardt (LM) method [30], [39] is used to reconstruct the unknown scatterer dielectric parameters based on the obtained sensitivity matrices. The computation accuracy and efficiency of the forward FEBI solvers are validated via comparing our results with the FEM simulations performed by the commercial software COMSOL with an ABC imposed. The feasibility of the inverse FEBI-LM solver is validated via the reconstruction of both isotropic and anisotropic inhomogeneous scatterers straddling multiple layers. One should note that our work is also different from [40] and [41] since they use the hybrid spectral-integral method (SIM) and SEM as the forward solver and the FWI is only performed in a homogeneous background medium. This leads to different system matrices in the forward scattering and also different sensitivity matrices in the FWI.

The rest of this article is organized as follows. In Sections II and III, the system matrices and the radiation matrices for the TE mode and the TM mode in the forward scattering computation and the sensitivity matrices for the TE mode and the TM mode in the FWI are derived, respectively. In Section IV, the correctness and efficiency of the forward scattering solvers for inhomogeneous isotropic and anisotropic objects straddling multiple planar layers are validated by comparing the computation results with the FEM simulations implemented by COMSOL with an ABC imposed. In Section V, the feasibility of the FWI solver based on the FEBI-LM algorithm to simultaneously reconstruct multiple scatterers straddling multiple planar layers is proved in two numerical experiments. Finally, in Section VI, the conclusion and summary are presented.

II. FORWARD PROBLEM FORMULATION

As shown in Fig. 1, several inhomogeneous scatterers are placed inside the computation domain V which straddles multiple background layers and is wrapped by a smooth boundary S. The forward scattering is formulated by the 2-D Helmholtz equation and solved by FEM in the domain V whose boundary S is formulated by a boundary IE which is solved by MoM. In the TE-mode configuration, we have $\mathbf{E} = \hat{y}E_y$ and $\mathbf{H} = \hat{x}H_x + \hat{z}H_z$. The transmitters are 2-D electric dipoles with $\mathbf{J} = \hat{y}J_y$. Both the inhomogeneous scatterers and the medium in each planar layer are isotropic and nonmagnetic, i.e., the relative permeability $\mu = 1$. By contrast, in the TM-mode configuration, we have $\mathbf{E} = \hat{x}E_x + \hat{z}E_z$ and $\mathbf{H} = \hat{y}H_y$. The transmitters are 2-D magnetic dipoles with $\mathbf{M} = \hat{y}M_y$. The medium in each planar layer is biaxially anisotropic with the complex relative permittivity tensor $\overline{\overline{\epsilon}}_b = \hat{x}\hat{x}\epsilon_x + \hat{z}\hat{z}\epsilon_z$.
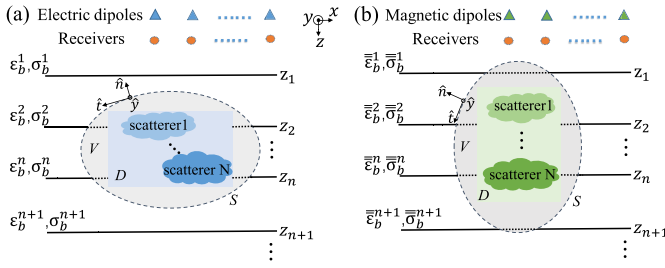
Fig. 1. Two-dimensional EM scattering and inverse scattering of multiple inhomogeneous scatterers straddling multiple planar layers solved by FEBI and LM methods. The FEBI is implemented inside the domain V wrapped by a smooth boundary S to compute the scattered fields at the receiver array. The LM is implemented in the region D embedded inside V to reconstruct the scatterer dielectric parameters. (a) TE mode with 2-D electric dipoles illuminating the isotropic scatterers. (b) TM mode with 2-D magnetic dipoles illuminating the anisotropic scatterers.

However, the scatterers are arbitrarily anisotropic and their complex relative permittivity tensors are constructed by

$$
\bar{\bar{\epsilon}}_s = \begin{bmatrix} \epsilon_{xx} & \epsilon_{xz} \\ \epsilon_{zx} & \epsilon_{zz} \end{bmatrix} = \boldsymbol{\Theta}^{-1} \begin{bmatrix} \epsilon_x & 0 \\ 0 & \epsilon_z \end{bmatrix} \boldsymbol{\Theta}
$$
$$
= \boldsymbol{\Theta}^{-1} \begin{bmatrix} \varepsilon_x + \dfrac{\sigma_x}{j\omega\varepsilon_0} & 0 \\ 0 & \varepsilon_z + \dfrac{\sigma_z}{j\omega\varepsilon_0} \end{bmatrix} \boldsymbol{\Theta} \quad (1)
$$

where

$$
\boldsymbol{\Theta} = \begin{bmatrix} \cos\theta & \sin\theta \\ -\sin\theta & \cos\theta \end{bmatrix} \quad (2)
$$

is the rotation matrix with θ the angle between the optical axis of the biaxially anisotropic medium and the positive $\hat{x}$-axis [42]. Then, the 2-D Helmholtz equation used to formulate the EM fields inside the computation domain D without internal excitation and the 1-D IE used to formulate the RBC can be written as

$$
-\nabla_t \times \left(\frac{1}{\mu}\nabla_t \times \hat{y}E_y\right) + k_0^2\epsilon \hat{y}E_y = 0 \quad (3a)
$$
$$
\frac{1}{2}\hat{y}E_y(\boldsymbol{\rho}) - \oint_S \bar{\bar{\mathbf{G}}}_{\mathbf{EM}}^h(\boldsymbol{\rho}, \boldsymbol{\rho}') \cdot \left[-\hat{n}(\boldsymbol{\rho}') \times \hat{y}E_y(\boldsymbol{\rho}')\right]dt'
$$
$$
-\oint_S \bar{\bar{\mathbf{G}}}_{\mathbf{EJ}}^h(\boldsymbol{\rho}, \boldsymbol{\rho}') \cdot \hat{y}J_y(\boldsymbol{\rho}')dt' = \hat{y}E_y^{\text{inc}}(\boldsymbol{\rho}) \quad (3b)
$$

for the TE mode and they can be written as

$$
-\nabla_t \times \left(\bar{\bar{\epsilon}}_t^{-1}\nabla_t \times \hat{y}H_y\right) + k_0^2\mu \hat{y}H_y = 0 \quad (4a)
$$
$$
\frac{1}{2}\hat{y}H_y(\boldsymbol{\rho}) - \oint_S \bar{\bar{\mathbf{G}}}_{\mathbf{HJ}}^e(\boldsymbol{\rho}, \boldsymbol{\rho}') \cdot \left[\hat{n}(\boldsymbol{\rho}') \times \hat{y}H_y(\boldsymbol{\rho}')\right]dt'
$$
$$
-\oint_S \bar{\bar{\mathbf{G}}}_{\mathbf{HM}}^e(\boldsymbol{\rho}, \boldsymbol{\rho}') \cdot \hat{y}M_y(\boldsymbol{\rho}')dt' = \hat{y}H_y^{\text{inc}}(\boldsymbol{\rho}) \quad (4b)
$$

for the TM mode.

Note in (3) and (4), $\nabla_t = \hat{x}(\partial/\partial x) + \hat{z}(\partial/\partial z)$ is the gradient in the xz-plane and $\oint$ is the Cauchy principal integral used to circumvent the singularity when the source point $\boldsymbol{\rho}'$ and the field point $\boldsymbol{\rho}$ overlap on S, $\hat{n}$ is the outward unit normal vector along the smooth boundary S as shown in Fig. 1, $\bar{\bar{\mathbf{G}}}_{\mathbf{EM}}$, $\bar{\bar{\mathbf{G}}}_{\mathbf{EJ}}$, $\bar{\bar{\mathbf{G}}}_{\mathbf{HJ}}$, and $\bar{\bar{\mathbf{G}}}_{\mathbf{HM}}$ are 2-D layered-medium dyadic Green's functions (DGFs) whose computation is discussed in

Appendix A, the superscript h stands for the TE mode, and the superscript e stands for the TM mode. Finally, we follow the similar derivation procedures presented in [40] and [41] to define $\overline{J}_y = \eta_0 J_y$ and $\overline{M}_y = (1/\eta_0)M_y$, discretize the domain V into several quadrilateral elements with N_i nodes, discretize the boundary S into N_b arc elements, expand E_y, $\overline{J}_y$, H_y, and $\overline{M}_y$ in (3) and (4) with the bilinear basis functions given in Appendix B, test both sides of (3) and (4) with the same functions, and come to the discretized algebraic equation

$$
\mathbf{Z}^h\mathbf{e} = \begin{bmatrix} \mathbf{Z}_{ii}^h & \mathbf{Z}_{ib}^h & \mathbf{0} \\ \mathbf{Z}_{bi}^h & \mathbf{Z}_{bb}^h & \mathbf{Z}_S^h \\ \mathbf{0} & \mathbf{Z}_M^h & \mathbf{Z}_J^h \end{bmatrix} \begin{bmatrix} \mathbf{e}_i \\ \mathbf{e}_b \\ \overline{\mathbf{J}}_b \end{bmatrix} = \begin{bmatrix} \mathbf{0} \\ \mathbf{0} \\ \mathbf{V}_S^h \end{bmatrix} = \mathbf{V}^h \quad (5)
$$

for the TE mode and

$$
\mathbf{Z}^e\mathbf{h} = \begin{bmatrix} \mathbf{Z}_{ii}^e & \mathbf{Z}_{ib}^e & \mathbf{0} \\ \mathbf{Z}_{bi}^e & \mathbf{Z}_{bb}^e & \mathbf{Z}_S^e \\ \mathbf{0} & \mathbf{Z}_J^e & \mathbf{Z}_M^e \end{bmatrix} \begin{bmatrix} \mathbf{h}_i \\ \mathbf{h}_b \\ \overline{\mathbf{M}}_b \end{bmatrix} = \begin{bmatrix} \mathbf{0} \\ \mathbf{0} \\ \mathbf{V}_S^e \end{bmatrix} = \mathbf{V}^e \quad (6)
$$

for the TM mode. Note in (5) and (6), the subscript i means inside the region V and the subscript b means on the boundary S. The source matrix $\mathbf{V}_S^h \in \mathbb{C}^{N_b \times N_T}$ is composed of E_y^{inc} values sampled at different discrete points at the smooth boundary S when N_T different electric dipoles, respectively, illuminate the region V. Similarly, $\mathbf{V}_S^e \in \mathbb{C}^{N_b \times N_T}$ is composed of H_y^{inc} values sampled on S when the sources are magnetic dipoles. The matrix $\mathbf{e}_i \in \mathbb{C}^{N_i \times N_T}$ is composed of the expansion coefficients of the total electric fields sampled at the internal nodes while $\mathbf{h}_i \in \mathbb{C}^{N_i \times N_T}$ is composed of the expansion coefficients of the total magnetic fields. The matrix $\mathbf{e}_b \in \mathbb{C}^{N_b \times N_T}$ is composed of the expansion coefficients of the total electric fields sampled at the boundary nodes while $\mathbf{h}_b \in \mathbb{C}^{N_b \times N_T}$ is composed of the expansion coefficients of the magnetic fields at the boundary nodes. The matrix $\overline{\mathbf{J}}_b \in \mathbb{C}^{N_b \times N_T}$ is composed of the expansion coefficients of the scaled equivalent electric current sampled at the boundary nodes while $\overline{\mathbf{M}}_b \in \mathbb{C}^{N_b \times N_T}$ is composed of the expansion coefficients of the scaled equivalent magnetic current at the boundary nodes. The matrix $\mathbf{Z}_{ii} \in \mathbb{C}^{N_i \times N_i}$ is assembled for the discretized elements inside the region V when both testing functions and basis functions act on the internal nodes. The matrix $\mathbf{Z}_{ib} \in \mathbb{C}^{N_i \times N_b}$ is assembled for the discretized elements at the boundary S when the basis functions act on the boundary nodes while the testing functions act on the internal nodes. The matrix $\mathbf{Z}_{bi} \in \mathbb{C}^{N_b \times N_i}$ is assembled for the discretized elements inside the region V but adjacent to the boundary S when the basis functions act on the internal nodes while the testing functions act on the boundary nodes. The matrices $\mathbf{Z}_{bb} \in \mathbb{C}^{N_b \times N_b}$ and $\mathbf{Z}_S \in \mathbb{C}^{N_b \times N_b}$ are assembled for the discretized elements on the boundary S when both testing functions and basis functions act on the boundary nodes. The matrices $\mathbf{Z}_J \in \mathbb{C}^{N_b \times N_b}$ and $\mathbf{Z}_M \in \mathbb{C}^{N_b \times N_b}$ are assembled by the 2-D layered-medium DGFs at the boundary S. The whole system matrix $\mathbf{Z}$ is a square matrix with the dimensions of $(N_i + 2N_b) \times (N_i + 2N_b)$.

Once the unknown matrix $\mathbf{e}$ or $\mathbf{h}$ is solved from (5) or (6), the scattered fields at the receiver array can be obtained by multiplying the radiation matrix by $\mathbf{e}$ or $\mathbf{h}$. They are

written as

$$\mathbf{E}_y^{\text{sct}} = \mathbf{R}^{E_y}\mathbf{e} = \begin{bmatrix} \mathbf{0} & \mathbf{R}_M^{E_y} & \mathbf{R}_J^{E_y} \end{bmatrix} \begin{bmatrix} \mathbf{e}_i \\ \mathbf{e}_b \\ \overline{\overline{\mathbf{J}}}_b \end{bmatrix} \quad (7a)$$

$$\mathbf{H}_x^{\text{sct}} = \mathbf{R}^{H_x}\mathbf{e} = \begin{bmatrix} \mathbf{0} & \mathbf{R}_M^{H_x} & \mathbf{R}_J^{H_x} \end{bmatrix} \begin{bmatrix} \mathbf{e}_i \\ \mathbf{e}_b \\ \overline{\overline{\mathbf{J}}}_b \end{bmatrix} \quad (7b)$$

$$\mathbf{H}_z^{\text{sct}} = \mathbf{R}^{H_z}\mathbf{e} = \begin{bmatrix} \mathbf{0} & \mathbf{R}_M^{H_z} & \mathbf{R}_J^{H_z} \end{bmatrix} \begin{bmatrix} \mathbf{e}_i \\ \mathbf{e}_b \\ \overline{\overline{\mathbf{J}}}_b \end{bmatrix} \quad (7c)$$

for the TE mode and

$$\mathbf{E}_x^{\text{sct}} = \mathbf{R}^{E_x}\mathbf{h} = \begin{bmatrix} \mathbf{0} & \mathbf{R}_J^{E_x} & \mathbf{R}_M^{E_x} \end{bmatrix} \begin{bmatrix} \mathbf{h}_i \\ \mathbf{h}_b \\ \overline{\overline{\mathbf{M}}}_b \end{bmatrix} \quad (8a)$$

$$\mathbf{E}_z^{\text{sct}} = \mathbf{R}^{E_z}\mathbf{h} = \begin{bmatrix} \mathbf{0} & \mathbf{R}_J^{E_z} & \mathbf{R}_M^{E_z} \end{bmatrix} \begin{bmatrix} \mathbf{h}_i \\ \mathbf{h}_b \\ \overline{\overline{\mathbf{M}}}_b \end{bmatrix} \quad (8b)$$

$$\mathbf{H}_y^{\text{sct}} = \mathbf{R}^{H_y}\mathbf{h} = \begin{bmatrix} \mathbf{0} & \mathbf{R}_J^{H_y} & \mathbf{R}_M^{H_y} \end{bmatrix} \begin{bmatrix} \mathbf{h}_i \\ \mathbf{h}_b \\ \overline{\overline{\mathbf{M}}}_b \end{bmatrix} \quad (8c)$$

for the TM mode. Note in (7) and (8), the radiation matrix $\mathbf{R}$ is mainly composed of 2-D layered-medium Green's functions linking the boundary nodes on S and the receivers. For example, $\mathbf{R}_M^{H_y}$ corresponds to the $\hat{y}\hat{y}$ component of $\overline{\overline{\mathbf{G}}}_{\text{HM}}^e$ whose computation is discussed in Appendix A. In addition, we assume there are totally N_R receivers. So, the radiation matrix $\mathbf{R}$ has the dimensions of $N_R \times (N_i + 2N_b)$. The field vectors $\mathbf{E}^{\text{sct}}$ and $\mathbf{H}^{\text{sct}}$ have the dimensions of $N_R \times N_T$.

III. INVERSE PROBLEM FORMULATION

As shown in Fig. 1, the FWI is implemented inside the rectangular region D whose boundary keeps at least one discrete element away from the smooth boundary S. In this way, only the $\mathbf{Z}_{ii}$ submatrix in the system matrix $\mathbf{Z}$ given in (5) or (6) is related to the unknown model parameters inside D. Computing the sensitivity matrix of the scattered field with respect to the model parameters is simplified. Now, we assume all the unknown model parameters are assembled into a vector $\mathbf{X}$, compactly rewrite the state equations (5) and (6) as

$$\mathbf{Zu} = \mathbf{V} \quad (9)$$

where $\mathbf{Z}$ can take $\mathbf{Z}^h$ or $\mathbf{Z}^e$, $\mathbf{u}$ can take $\mathbf{e}$ or $\mathbf{h}$, and $\mathbf{V}$ can take $\mathbf{V}^h$ or $\mathbf{V}^e$, and compactly rewrite the data equations (7) and (8) as

$$\mathbf{F}^{\text{sct}} = \mathbf{Ru} \quad (10)$$

where $\mathbf{F}^{\text{sct}}$ can take $\mathbf{E}_y^{\text{sct}}$, $\mathbf{H}_x^{\text{sct}}$, $\mathbf{H}_z^{\text{sct}}$, $\mathbf{E}_x^{\text{sct}}$, $\mathbf{E}_z^{\text{sct}}$, or $\mathbf{H}_y^{\text{sct}}$, and $\mathbf{R}$ can take $\mathbf{R}^{E_y}$, $\mathbf{R}^{H_x}$, $\mathbf{R}^{H_z}$, $\mathbf{R}^{E_x}$, $\mathbf{R}^{E_z}$, or $\mathbf{R}^{H_y}$. Note in (9) or (10), $\mathbf{V}$ is composed of incident fields at the boundary S and thus is independent of the unknown model parameters. $\mathbf{R}$ is composed of 2-D layered-medium DGFs and thus is also independent of the unknown model parameters. In addition, it should be emphasized again $\mathbf{Z}$ is a square matrix. Then,

by taking the derivatives of both sides of (9) and (10) with respect to $\mathbf{X}$, we obtain

$$\frac{\partial \mathbf{Z}}{\partial \mathbf{X}}\mathbf{u} + \mathbf{Z}\frac{\partial \mathbf{u}}{\partial \mathbf{X}} = \mathbf{0} \quad (11)$$

and

$$\frac{\partial \mathbf{F}^{\text{sct}}}{\partial \mathbf{X}} = \mathbf{R}\frac{\partial \mathbf{u}}{\partial \mathbf{X}}. \quad (12)$$

In the next step, we substitute $(\partial \mathbf{u}/\partial \mathbf{X})$ solved from (11) into (12), take the transposes of both sides of (12), and finally come to

$$\left(\frac{\partial \mathbf{F}^{\text{sct}}}{\partial \mathbf{X}}\right)^{\text{T}} = -\left(\frac{\partial \mathbf{Z}}{\partial \mathbf{X}}\mathbf{u}\right)^{\text{T}}(\mathbf{Z}^{\text{T}})^{-1}\mathbf{R}^{\text{T}} \quad (13)$$

where the order of matrix inverse and transpose has been interchanged. Note $(\mathbf{Z}^{\text{T}})^{-1}\mathbf{R}^{\text{T}}$ in (13) is actually the adjoint field solution which is denoted as $\mathbf{u}^*$ in the following derivations. We then substitute $\mathbf{u}^*$ into (13), take the transposes of two sides again, and come to

$$\frac{\partial \mathbf{F}^{\text{sct}}}{\partial \mathbf{X}} = -(\mathbf{u}^*)^{\text{T}}\frac{\partial \mathbf{Z}}{\partial \mathbf{X}}\mathbf{u}. \quad (14)$$

In the following, we will discuss the computation of $(\partial \mathbf{Z}/\partial \mathbf{X})$ and the assembly of the sensitivity matrix for the TE mode and the TM mode, respectively.

A. Assembly of the Sensitivity Matrix for TE Mode

We denote the complex relative permittivity ϵ in the mth discrete quadrilateral element inside the region D as x_m. Because all the quadrilateral elements inside D are not in touch with the boundary S, $(\partial \mathbf{Z}^h/\partial \mathbf{X})$ only depends on $(\partial \mathbf{Z}_{ii}^h/\partial \mathbf{X})$. By referring to (3a), we can see that only the mass matrix in $\mathbf{Z}_{ii}^h$ is related to the unknown ϵ. Therefore, we only keep the mass matrix and write the weak form of $\mathbf{Z}_{ii}^h$ in the physical coordinate as

$$Z_{ii,pq}^h = \int_V k_0^2 \epsilon \psi_p(x,z)\psi_q(x,z)dxdz \quad (15)$$

where ψ_q is the qth basis function and ψ_p is the pth testing function. Note the integration in (15) is difficult to perform in an irregular quadrilateral element. We transform it to the reference domain by

$$Z_{ii,pq}^h(i,j) = \iint_{-1}^1 k_0^2 \epsilon \phi_i(\xi,\eta)\phi_j(\xi,\eta)|\mathbf{J}(\xi,\eta)|d\xi d\eta \quad (16)$$

where $i \in [1, 4]$ is the index of the bilinear testing function in the reference domain for ψ_p while $j \in [1, 4]$ is the index of the bilinear basis function in the reference domain for ψ_q. $|\mathbf{J}(\xi,\eta)|$ is the determinant of the Jacobian matrix $\mathbf{J}$ used for coordinate system transform. The expressions of $\phi_i(\xi,\eta)$ and $\phi_j(\xi,\eta)$ are given in Appendix B. We then compute the derivative of $Z_{ii,pq}^h$ in (16) with respect to the model parameter x_m, i.e., ϵ, in the mth discrete quadrilateral element, perform the double integration using the 2-D third-order Legendre–Gauss quadrature, and come to

$$\frac{\partial Z_{ii,pq}^h(i,j)}{\partial x_m} = k_0^2 \sum_{k=1}^9 \phi_i(\xi_k,\eta_k)\phi_j(\xi_k,\eta_k)|\mathbf{J}(\xi_k,\eta_k)|w_{k_\xi}w_{k_\eta}$$

$$(17)$$

where k is the index for 2-D Legendre–Gauss quadrature point and w_{k_ξ} and w_{k_η} are the corresponding weights in the $\hat{\xi}$-direction and $\hat{\eta}$-direction, respectively. One should note $(\partial Z_{ii,pq}^h(i,j)/\partial x_m)$ corresponds to one of the 4×4 elements most of which are not zero since the Legendre–Gauss quadrature point does not coincide with the vertex of the quadrilateral element. We now number the four vertexes of the mth quadrilateral element as p_1, p_2, p_3, and p_4 in all the discrete nodes of the whole computation domain and denote the solution of the state equation (5) when the inversion domain D is illuminated by the tth electric dipole as $\mathbf{e}_t$. The multiplication of $(\partial \mathbf{Z}^h/\partial x_m)$ and $\mathbf{e}_t$ is evaluated by

$$\left(\frac{\partial \mathbf{Z}^h}{\partial x_m}\mathbf{e}_t\right)_{p_i} = \sum_{j=1}^{4} \frac{\partial Z_{ii,pq}^h(i,j)}{\partial x_m}(\mathbf{e}_t)_{p_j} \tag{18}$$

where $(\partial \mathbf{Z}^h/\partial x_m)\mathbf{e}_t$ has the dimensions of $(N_i + 2N_b) \times 1$ and only the four elements located at the positions of p_1, p_2, p_3, and p_4 are not zero. On the other hand, the adjoint solution $\mathbf{e}^*$ when the inversion domain D is illuminated by the rth receiver has the dimensions of $(N_i + 2N_b) \times 1$. By referring to (14), we can see that $(\mathbf{e}^*)^{\mathrm{T}}$ only interacts with the four nonzero elements of $(\partial \mathbf{Z}^h/\partial x_m)\mathbf{e}_t$. Therefore, by substituting (17) into (18) and substituting (18) into (14), we obtain the TE-mode sensitivity matrix term for the mth quadrilateral element when the inversion domain is illuminated by the tth electric dipole and the scattered electric field is recorded at the rth receiver

$$\frac{\partial F_{r,t}^{\mathrm{sct}}}{\partial x_m}$$
$$= -\sum_{i=1}^{4}\left[(\mathbf{e}^*)^{\mathrm{T}}\right]_{r,p_i}$$
$$\times \sum_{j=1}^{4}\left\{k_0^2 \sum_{k=1}^{9} \phi_i(\xi_k,\eta_k)\phi_j(\xi_k,\eta_k)|\mathbf{J}(\xi_k,\eta_k)|w_{k_\xi}w_{k_\eta}\right\}(\mathbf{e}_t)_{p_j} \tag{19}$$

where F^{sct} only takes E_y^{sct}. The final sensitivity matrix is assembled by letting m traverse all the FEM quadrilateral elements, r traverse all receivers, and t traverse all transmitters.

B. Assembly of the Sensitivity Matrix for TM Mode

For the TM mode, by referring to (4a), we only keep the stiffness matrix and write the weak form of $\mathbf{Z}_{ii}^e$ in the physical coordinate as

$$Z_{ii,pq}^e = \int_V -(\hat{y} \times \nabla_t \psi_p(x,z)) \cdot \overline{\overline{\epsilon}}_t^{-1}(\hat{y} \times \nabla_t \psi_q(x,z))dxdz \tag{20}$$

which can be further transformed to the reference domain by

$$Z_{ii,pq}^e(i,j)$$
$$= \iint_{-1}^{1} -\left(\hat{y} \times \mathbf{J}^{-1}\nabla_t'\phi_i(\xi,\eta)\right)$$
$$\cdot \overline{\overline{\epsilon}}_t^{-1}\left(\hat{y} \times \mathbf{J}^{-1}\nabla_t'\phi_j(\xi,\eta)\right)|\mathbf{J}(\xi,\eta)|d\xi d\eta \tag{21}$$

where $\nabla_t' = \hat{\xi}(\partial/\partial\xi) + \hat{\eta}(\partial/\partial\eta)$ is the gradient operator in the $\xi\eta$ domain and $\hat{y}\times$ can be replaced with $\begin{bmatrix} 0 & 1 \\ -1 & 0 \end{bmatrix}$ for a 2-D problem. In the next step, we still use the 2-D third-order Legendre–Gauss quadrature to numerically evaluate the double integral in (21), invoke the equivalent model parameter definition for the derivatives of $\overline{\overline{\epsilon}}_t^{-1}$ with respect to ϵ_x, ϵ_z, and θ defined in [41, eq. (29)], and come to

$$\frac{\partial Z_{ii,pq}^e(i,j)}{\partial x_m}$$
$$= \sum_{k=1}^{9} -\left(\begin{bmatrix} 0 & 1 \\ -1 & 0 \end{bmatrix} \cdot \left[\mathbf{J}^{-1}\nabla_t'\phi_i\right]_{\xi_k,\eta_k}\right)$$
$$\cdot \boldsymbol{\Theta}^{-1}\mathbf{m}^{eq}\boldsymbol{\Theta}\left(\begin{bmatrix} 0 & 1 \\ -1 & 0 \end{bmatrix} \cdot \left[\mathbf{J}^{-1}\nabla_t'\phi_j\right]_{\xi_k,\eta_k}\right)|\mathbf{J}(\xi_k,\eta_k)|w_{k_\xi}w_{k_\eta} \tag{22}$$

where x_m can take ϵ_x, ϵ_z, or θ and $\mathbf{m}^{eq}$ correspondingly takes

$$\begin{bmatrix} -\dfrac{1}{\epsilon_x^2} & 0 \\ 0 & 0 \end{bmatrix}, \quad \begin{bmatrix} 0 & 0 \\ 0 & -\dfrac{1}{\epsilon_z^2} \end{bmatrix}, \quad \text{or} \quad \begin{bmatrix} 0 & \dfrac{1}{\epsilon_x} - \dfrac{1}{\epsilon_z} \\ \dfrac{1}{\epsilon_x} - \dfrac{1}{\epsilon_z} & 0 \end{bmatrix}.$$

We then perform the multiplication similar to that in (18) and obtain

$$\left(\frac{\partial \mathbf{Z}^e}{\partial x_m}\mathbf{h}_t\right)_{p_i} = \sum_{j=1}^{4} \frac{\partial Z_{ii,pq}^e(i,j)}{\partial x_m}(\mathbf{h}_t)_{p_j} \tag{23}$$

where $\mathbf{h}_t$ is the solution of the state equation (6) when the inversion domain D is illuminated by the tth magnetic dipole. Finally, by substituting (22) into (23) and substituting (23) into (14), we obtain the TM-mode sensitivity matrix term for the mth quadrilateral element when the inversion domain is illuminated by the tth magnetic dipole and the scattered electric field is recorded at the rth receiver

$$\frac{\partial F_{r,t}^{\mathrm{sct}}}{\partial x_m}$$
$$= \sum_{i=1}^{4}\left[(\mathbf{h}^*)^{\mathrm{T}}\right]_{r,p_i}$$
$$\sum_{j=1}^{4}\left\{\sum_{k=1}^{9}\left(\begin{bmatrix} 0 & 1 \\ -1 & 0 \end{bmatrix} \cdot \left[\mathbf{J}^{-1}\nabla_t'\phi_i\right]_{\xi_k,\eta_k}\right) \cdot \boldsymbol{\Theta}^{-1}\mathbf{m}^{eq}\boldsymbol{\Theta}\right.$$
$$\left.\left(\begin{bmatrix} 0 & 1 \\ -1 & 0 \end{bmatrix} \cdot \left[\mathbf{J}^{-1}\nabla_t'\phi_j\right]_{\xi_k,\eta_k}\right)|\mathbf{J}(\xi_k,\eta_k)|w_{k_\xi}w_{k_\eta}\right\}(\mathbf{h}_t)_{p_j} \tag{24}$$

where F^{sct} can take E_x^{sct} or E_z^{sct} and the corresponding adjoint field $\mathbf{h}^*$ is solved for when the scattered field is transmitted from the receiver array.

C. Implementation of FWI

The sensitivity matrix terms computed by (19) and (24) are complex values. The corresponding real terms for the real relative permittivity and the angle θ can be obtained by properly detaching the real and imaginary parts of both $F_{r,t}^{\mathrm{sct}}$ and $(\partial F_{r,t}^{\mathrm{sct}}/\partial x_m)$ in (19) and (24). Following this, we can
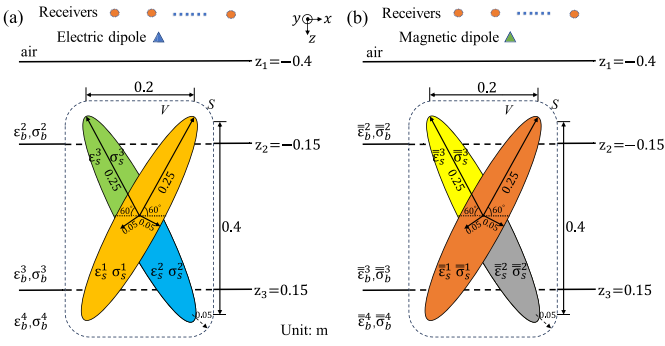
Fig. 2. Forward scattering computation models including two overlapped tilted ellipses straddling multiple planar layers. (a) Isotropic ellipses are illuminated by TE waves excited by an electric dipole. (b) Anisotropic ellipses are illuminated by TM waves excited by a magnetic dipole. The boundary integration is implemented on the smooth rounded rectangle S. The EM fields in the inhomogeneous region inside S are evaluated by FEM.

construct the first-order real sensitivity matrix $(\partial \mathbf{F}'^{\text{sct}}/\partial \mathbf{X}')$ which is also called Jacobian matrix in literature and denoted as $\mathbf{S}$ in the following derivation. Note $\mathbf{F}'^{\text{sct}}$ is assembled from the real part and the imaginary part of $\mathbf{F}^{\text{sct}}$ in (14) while $\mathbf{X}'$ is assembled from the real part and the imaginary part of $\mathbf{X}$ in (14). Then, the least square cost function is constructed as

$$C(\mathbf{X}') = \left\| \mathbf{F}'^{\text{sct}}_{\text{mea}} - \mathbf{F}'^{\text{sct}}(\mathbf{X}') \right\|^2 \tag{25}$$

where $\|\cdot\|$ represents the L_2 norm, $\mathbf{F}'^{\text{sct}}_{\text{mea}}$ represents the scattered field data measured at the receiver array, and $\mathbf{F}'^{\text{sct}}$ stands for the scattered field data computed by the forward scattering model. Finally, in order to find the optimized solution of $\mathbf{X}'$ to minimize C in (25), we follow the derivation procedure of LM algorithm given in [39], expand $\mathbf{F}'^{\text{sct}}$ by the first-order Taylor series with respect to the increment $\delta\mathbf{X}'$ in each iteration step, compute the first-order derivative of C with respect to $\mathbf{X}'$ and let it be zero, and come to

$$\left[\mathbf{S}^{\text{T}}\mathbf{S} + \gamma \text{diag}(\mathbf{S}^{\text{T}}\mathbf{S})\right]\delta\mathbf{X}' = \mathbf{S}^{\text{T}}\left[\mathbf{F}'^{\text{sct}}_{\text{mea}} - \mathbf{F}'^{\text{sct}}(\mathbf{X}')\right] \tag{26}$$

where γ is a damping factor. We choose it according to the strategy given in [43], make slight modifications, and construct it as

$$\gamma = \left(\frac{\left\| \mathbf{F}'^{\text{sct}}_{\text{mea}} - \mathbf{F}'^{\text{sct}}(\mathbf{X}') \right\|}{\left\| \mathbf{F}'^{\text{sct}}_{\text{mea}} \right\|} \right)^n \tag{27}$$

where n is the power which is empirically selected as 1.5 in this work. Once the increment $\delta\mathbf{X}'$ is solved for from (26) by conjugate gradient, we update $\mathbf{X}'$, implement the forward scattering computation $\mathbf{F}'^{\text{sct}}(\mathbf{X}')$, update the sensitivity matrix $\mathbf{S}$, and come to (26) again. This alternative iteration continues until the misfit between the measured scattered field data and the computed data becomes less than a prescribed threshold or the iteration number reaches a maximum value. In addition, the structural consistency constraint (SCC) is adopted to filter out the clutters of the background medium in the iteration process. Note the details of SCC can be found in [44] and its feasibility has been validated in our previous works [40], [41].

IV. FORWARD VALIDATION

In this section, we prove the superiority of our FEBI solver over the traditional FEM algorithm for the computation of

TABLE I
ANISOTROPIC DIELECTRIC PARAMETERS OF THE LAYERED BACKGROUND MEDIUM AND THE SCATTERERS SHOWN IN FIG. 2(b)

	ε_x	ε_y	σ_x	σ_y	θ
$\overline{\overline{\varepsilon}}_b^2$ & $\overline{\overline{\sigma}}_b^2$	1.3	1.6	1.0	2.0	0.0
$\overline{\overline{\varepsilon}}_b^3$ & $\overline{\overline{\sigma}}_b^3$	1.7	1.2	2.0	3.0	0.0
$\overline{\overline{\varepsilon}}_b^4$ & $\overline{\overline{\sigma}}_b^4$	2.3	2.7	3.0	4.0	0.0
$\overline{\overline{\varepsilon}}_s^1$ & $\overline{\overline{\sigma}}_s^1$	4.0	4.5	10.0	12.0	$-\frac{\pi}{6}$
$\overline{\overline{\varepsilon}}_s^2$ & $\overline{\overline{\sigma}}_s^2$	4.0	3.5	10.0	8.0	$\frac{\pi}{4}$
$\overline{\overline{\varepsilon}}_s^3$ & $\overline{\overline{\sigma}}_s^3$	3.5	3.0	9.0	6.0	$\frac{\pi}{6}$

Remark: the unit of σ is mS/m; the unit of θ is rad.

forward scattering from inhomogeneous objects embedded inside multiple subsurface planar layers by comparing our results with COMSOL simulation with a perfectly matched layer (PML) imposed on the computational domain boundary. Fig. 2(a) and (b) shows the representative scattering configurations for the TE mode and TM mode, respectively. The geometry parameters including the layer configurations, scatterer sizes, positions, etc. are the same for the two modes and they are annotated in the subfigures. However, the dielectric parameters are completely different. The TE mode has the isotropic dielectric parameters $\varepsilon_b^2 = 1.5$, $\varepsilon_b^3 = 2.0$, $\varepsilon_b^4 = 2.5$, $\varepsilon_s^1 = 4.0$, $\varepsilon_s^2 = 3.5$, $\varepsilon_s^3 = 3.0$, $\sigma_b^2 = 1.0$ mS/m, $\sigma_b^3 = 2.0$ mS/m, $\sigma_b^4 = 3.0$ mS/m, $\sigma_s^1 = 10.0$ mS/m, $\sigma_s^2 = 8.0$ mS/m, and $\sigma_s^3 = 6.0$ mS/m. Note the first layer for the TE mode is air. Similarly, for the TM mode, except for the first background layer which is also air, the anisotropic dielectric parameters of other layers and the scatterers are listed in Table I. Both the unit electric dipole transmitter in the TE mode and the unit magnetic dipole transmitter in the TM mode are located at $(0.0, -0.6)$ m. For either the TE mode or the TM mode, totally 49 receivers are evenly placed on a horizontal line at $z = -0.8$ m. The coordinate of the first receiver is $(-2.4, -0.8)$ m and the increment between two adjacent receivers is 0.1 m. The operation frequency is 1 GHz. The FEBI is implemented in the region V shown in Fig. 2. By contrast, the computational domain of COMSOL is a rectangle with the size of 5.6×1.65 m which actually also wraps the receiver array. The PML thickness is 0.15 m. All the simulations and numerical computations are performed on a workstation with an 18-core I9-10980XE 3.0 G CPU and 256 GB RAM.

Figs. 3 and 4 show the comparisons of computed scattered fields at the receiver array by FEBI method and by FEM with PMLs for the representative scattering configurations shown in Fig. 2. We can see that the results of our method match well with those from commercial software simulations. In the TE mode when the media are isotropic, the relative errors of E_y^{sct}, H_x^{sct}, and H_z^{sct} by FEBI method with respect to those by FEM with PMLs are 0.73%, 0.74%, and 0.69%, respectively. In the TM mode when the media are anisotropic, the relative errors of E_x^{sct}, E_z^{sct}, and H_y^{sct} by FEBI method with respect to those by FEM with PMLs are 1.8%, 1.1%, and 1.6%, respectively. Now, let us discuss the memory and time cost of two methods for two modes. Numerical simulations show that, for the TE mode with isotropic media, the FEBI method only needs 2.1-GB memory and 8.7 s to accomplish the computation but the FEM with PMLs consumes 16.6-GB memory
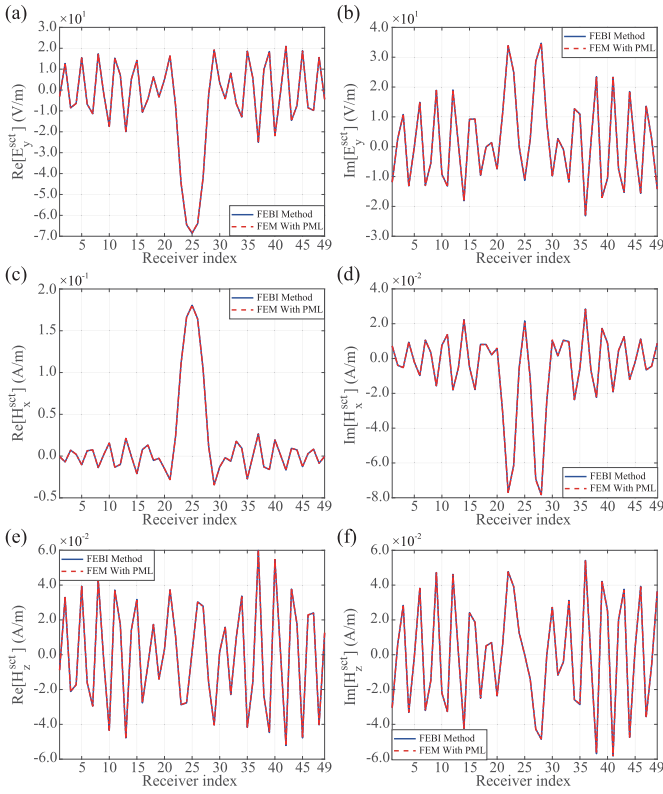
Fig. 3. Comparisons of the TE-mode scattered EM fields at the receiver array computed by FEBI method and FEM with PMLs. (a) Real part of E_y^{sct}. (b) Imaginary part of E_y^{sct}. (c) Real part of H_x^{sct}. (d) Imaginary part of H_x^{sct}. (e) Real part of H_z^{sct}. (f) Imaginary part of H_z^{sct}.

Fig. 4. Comparisons of the TM-mode scattered EM fields at the receiver array computed by FEBI method and FEM with PMLs. (a) Real part of E_x^{sct}. (b) Imaginary part of E_x^{sct}. (c) Real part of E_z^{sct}. (d) Imaginary part of E_z^{sct}. (e) Real part of H_y^{sct}. (f) Imaginary part of H_y^{sct}.

and 98 s. For the TM mode with anisotropic media, the FEBI method only needs 2.2-GB memory and 9.8 s to accomplish the computation but the FEM with PMLs consumes 17.1-GB memory and also 98 s. These error, memory, and time data indicate that our FEBI method can obtain reliable computing results for EM scattering from inhomogeneous isotropic and anisotropic objects straddling multiple subsurface planar layers but with a much lower consumption of computation resources compared with FEM with PMLs. In addition, it is worth noting that the relative computation errors between the FEBI method and FEM with PMLs are smaller for the TE mode with isotropic media compared with those for the TM mode with anisotropic media. The possible reason is that the anisotropy actually increases the complexity of the media spatial distribution, which naturally increases the numerical errors of 2-D layered-medium DGFs and thus the errors of FEBI results. Meanwhile, the FEBI method also consumes slightly more memory and time for the TM case compared with the TE case. The reason is similar to that mentioned above. The complexity caused by anisotropy also leads to more consumption of memory and time.

V. INVERSION ASSESSMENT

In this section, we verify the feasibility of EM FWI based on the proposed FEBI forward solver and the LM inversion algorithm to reconstruct both isotropic scatterers straddling multiple isotropic subsurface planar layers in the TE mode and arbitrarily anisotropic scatterers straddling multiple biaxially
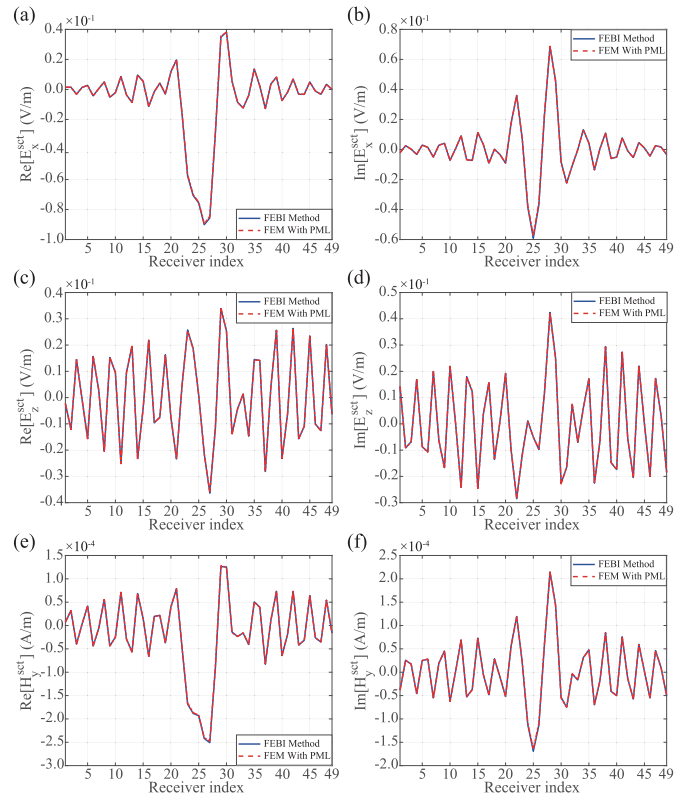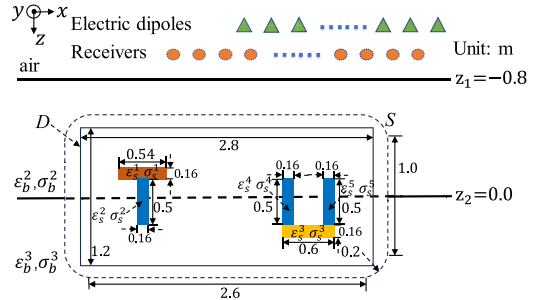

Fig. 5. Configuration of the 2-D FWI model in the TE mode. Both the isotropic inhomogeneous "T" shape scatterer and the "U" shape scatterer straddle two subsurface isotropic planar layers. Their geometry sizes are annotated in the figure. The FWI is performed in the rectangular region D.

anisotropic subsurface planar layers in the TM mode. The measured scattered field data recorded at the receiver array are simulated by the FEBI forward solver which has been validated in Section IV. Both the noise-free and noisy cases are tried. The white Gaussian noise level is defined according to the signal-to-noise ratio (SNR) of power. Therefore, 20-dB noise corresponds to approximately 10% errors of the scattered field data. In the first numerical example for the TE mode, the relative permittivity ε and the conductivity σ of scatterers are simultaneously retrieved. In the second numerical example for the TM mode, five model parameters ε_x, ε_y, σ_x, σ_y, and the rotation angle θ defined in (2) are simultaneously retrieved. In addition, we use the data misfit and model misfit defined in [41, eq. (34)] to quantitatively evaluate the mismatches between the computed scattered field
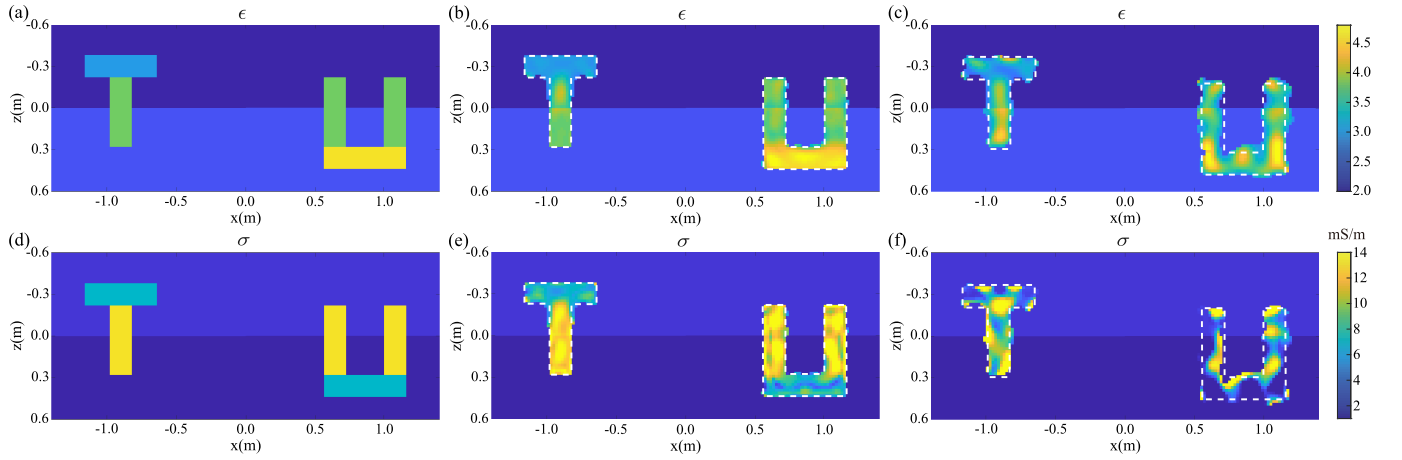
Fig. 6. Reconstructed isotropic profiles of the inhomogeneous "T" shape and "U" shape scatterers straddling the second and the third layers. The first column shows the ground truth profiles. The second column shows the reconstructed profiles when it is noise-free. The third column shows the reconstructed profiles when 20-dB noise is added. White dotted boxes denote true shapes.

data and the measured ones and the mismatches between the retrieved model parameters of scatterers and their true parameters. The stop criterion of the FWI iteration for the noise-free case is that the data misfit is less than 3×10^{-4} and there are no "background" pixels removed by SCC in four consecutive steps. However, for the noisy case, the stop criterion is that the data misfit approaches the noise level and there are no "background" pixels removed in four consecutive iterative steps.

A. FWI of Isotropic Scatterers in the TE Mode

As shown in Fig. 5, the background medium is isotropic and has three layers. The positions of the layer boundaries are annotated in the figure. The first layer is air. Other layers have the dielectric parameters $\varepsilon_b^2 = 2.0$, $\sigma_b^2 = 2.0$ mS/m, $\varepsilon_b^3 = 2.4$, and $\sigma_b^3 = 1.0$ mS/m. Both the "T" shape and the "U" shape scatterers straddle the second and the third subsurface layers and their geometry parameters are also annotated in the figure. Their center coordinates are $(-0.9, -0.13)$ m and $(0.86, 0.2)$ m, respectively. Their dielectric parameters are $\varepsilon_s^1 = 3.0$, $\sigma_s^1 = 7.0$ mS/m, $\varepsilon_s^2 = \varepsilon_s^4 = \varepsilon_s^5 = 3.8$, $\sigma_s^2 = \sigma_s^4 = \sigma_s^5 = 13.0$ mS/m, $\varepsilon_s^3 = 4.6$, and $\sigma_s^3 = 7.0$ mS/m. The FWI is performed in the rectangular domain D which has the size of 2.8×1.2 m and is uniformly discretized into 140×60 square elements. The forward scattering computation based on the FEBI method in each iteration of FWI is implemented in the region inside the smooth rounded rectangle S whose size is also annotated in Fig. 5. We evenly place 40 electric dipole transmitters on the horizontal line at $z = -1.0$ m and evenly place 60 receivers on the horizontal line at $z = -0.9$ m in the first layer. The coordinate of the first transmitter is $(-7.8, -1.0)$ m and the increment between two adjacent transmitters is 0.4 m. The coordinate of the first receiver is $(-11.8, -0.9)$ m and the increment between two adjacent receivers is also 0.4 m. The operation frequency is 300 MHz.

Fig. 6 shows the true relative permittivity and conductivity profiles of the "T" shape and the "U" shape as well as their reconstructed profiles when it is noise-free and the scattered field data are contaminated by 20-dB noise. The LM takes 269 iterations to decrease the data misfit to 0.0017% and
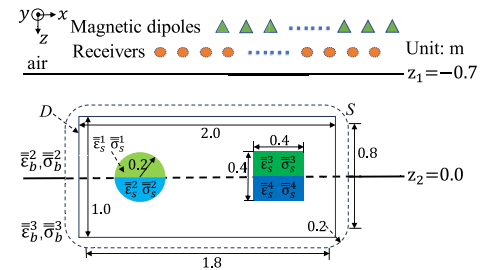

Fig. 7. Configuration of the 2-D FWI model in the TM mode. Both the arbitrarily anisotropic circular disk and the square straddle two subsurface biaxially anisotropic planar layers. Their geometry sizes are annotated in the figure. The FWI is implemented in the rectangular region D.

TABLE II
ANISOTROPIC DIELECTRIC PARAMETERS OF THE LAYERED BACKGROUND MEDIUM AND THE SCATTERERS SHOWN IN FIG. 7

	ε_x	ε_y	σ_x	σ_y	θ
$\overline{\overline{\varepsilon}}_b^2$ & $\overline{\overline{\sigma}}_b^2$	1.6	2.0	1.0	2.0	0.0
$\overline{\overline{\varepsilon}}_b^3$ & $\overline{\overline{\sigma}}_b^3$	2.0	2.4	2.0	1.0	0.0
$\overline{\overline{\varepsilon}}_s^1$ & $\overline{\overline{\sigma}}_s^1$	2.6	3.6	13.0	11.0	$\frac{\pi}{6}$
$\overline{\overline{\varepsilon}}_s^2$ & $\overline{\overline{\sigma}}_s^2$	3.3	4.3	8.0	6.0	$\frac{\pi}{6}$
$\overline{\overline{\varepsilon}}_s^3$ & $\overline{\overline{\sigma}}_s^3$	2.6	3.6	13.0	11.0	$-\frac{\pi}{6}$
$\overline{\overline{\varepsilon}}_s^4$ & $\overline{\overline{\sigma}}_s^4$	3.3	4.3	8.0	6.0	$-\frac{\pi}{6}$

Remark: the unit of σ is mS/m; the unit of θ is rad.

obtain the reconstructed profiles shown in Fig. 6 when it is noise-free but only takes 161 iterations to obtain the final reconstructed profiles when 20-dB noise is added. The model misfits of reconstructed permittivity profiles are 2.6% for the noise-free case and 12.7% for the noisy case. The corresponding model misfits of the reconstructed conductivity profiles are 4.7% and 37.5%, respectively. By comparing the profiles shown in the second column and the third column and those shown in the first column of Fig. 6, we can see the proposed FEBI-LM solver is able to reliably reconstruct both the shapes and inhomogeneous dielectric parameter distribution of multiple isotropic scatterers straddling multiple planar layers when it is noise-free. When 20-dB noise is added, although obvious distortions show up in the reconstruction, the basic shapes of the scatterers are still discernible and the boundaries between different homogeneous regions inside scatterers are also can
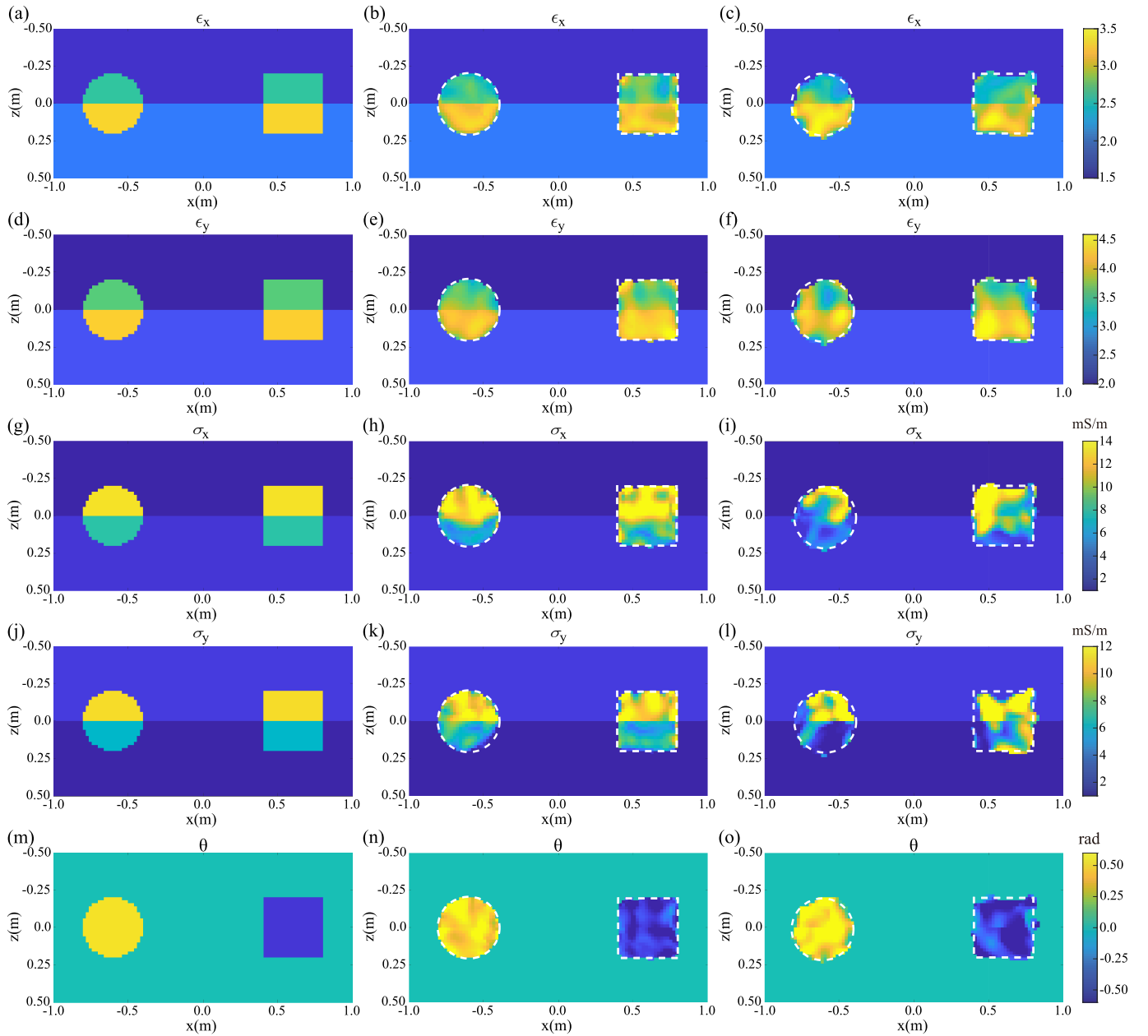
Fig. 8. Reconstructed dielectric biaxial parameters and rotation angles of the optical axes of the 2-D arbitrarily anisotropic scatterers straddling the second and the third layers. The first column shows the ground truth profiles. The second column shows the reconstructed profiles when it is noise-free. The third column shows the reconstructed profiles when 20-dB noise is added. White dotted boxes denote true shapes.

be found in the reconstructed permittivity profiles, as shown in Fig. 6(c). This indicates that our FEBI-LM solver has a certain antinoise ability. Note the reconstructed conductivity profile is obviously worse than the permittivity profile for the noisy case, as shown in Fig. 6(f). The possible reason is that the imaginary part of the complex permittivity is obviously smaller than its real part and thus the influence of conductivity on the scattered fields is even weaker than that from the external noise. Another interesting observation is that the background layer interface is coupled into the reconstructed profiles. Both the reconstructed "T" shape and "U" shape scatterers show slight discontinuities near the layer interface. This is because the interface also reflects EM waves. As a result, the FEBI-LM solver treats the interface as a scatterer and overlaps it with the true scatterer profiles.

B. FWI of Anisotropic Scatterers in the TM Mode

As shown in Fig. 7, the biaxially anisotropic background medium has three planar layers. The arbitrarily anisotropic inhomogeneous circular disk and square straddle the subsurface second and third layers. The positions of the background layer boundaries and the geometry sizes of two scatterers are annotated in Fig. 7. The center coordinates of the circular disk and the square are $(-0.6, 0.0)$ m and $(0.6, 0.0)$ m, respectively. The first layer of the background medium is air. The dielectric parameters of other layers and the scatterers are listed in Table II. The FWI is also implemented in the rectangular domain D with a size of 2.0×1.0 m which is uniformly discretized into 200×100 square elements, as shown in Fig. 7. Note the domain D is enclosed by the rounded rectangle S within which the forward scattering computation is performed.
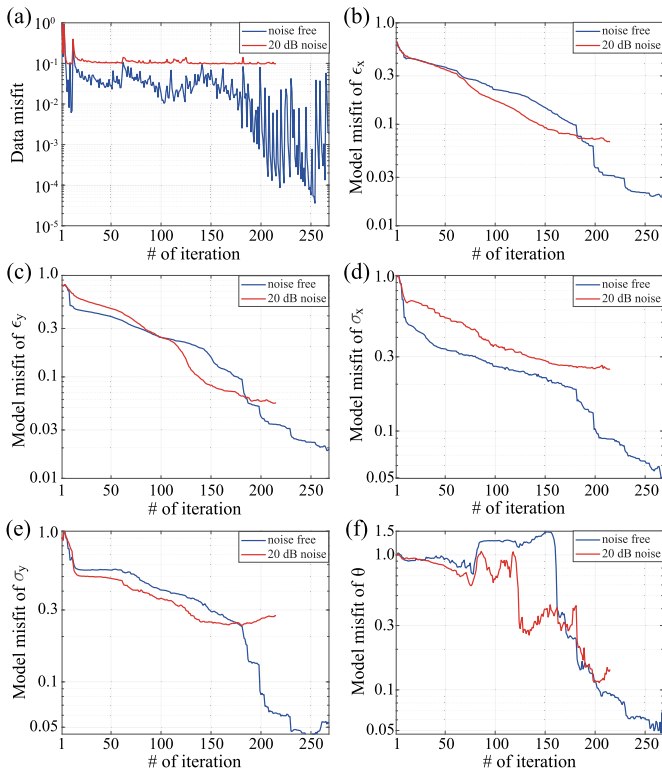
Fig. 9. Convergence processes for the FWI of multiple arbitrarily anisotropic scatterers straddling multiple subsurface planar layers. (a) Variations of data misfits of the scattered fields in different iteration steps. (b) Variations of model misfits of ε_x in different iteration steps. (c) Variations of model misfits of ε_y in different iteration steps. (d) Variations of model misfits of σ in different iteration steps. (e) Variations of model misfits of σ_y in different iteration steps. (f) Variations of model misfits of θ in different iteration steps.

Totally, 50 magnetic dipole transmitters are evenly placed on a horizontal line at $z = -0.9$ m while 60 receivers are evenly placed on a horizontal line at $z = -0.8$ m. The coordinates of the first transmitter and the first receiver are $(-9.8, -0.9)$ m and $(-11.8, -0.8)$ m, respectively. The interval between two adjacent transmitters or receivers is 0.4 m. The operation frequency is still 300 MHz.

Fig. 8 shows the ground truth profiles, the reconstructed profiles when it is noise-free, and the reconstructed profiles with 20-dB noise added of the five anisotropic parameters for the inhomogeneous circular disk and the square straddling two subsurface layers. We can see that our FEBI-LM solver can reliably retrieve multiple anisotropic parameters when the scatterers straddle multiple background layers. Especially, when it is noise-free, the shapes of two scatterers are well reconstructed and the boundary between two homogeneous parts of each scatterer for the permittivity and conductivity distribution is clearly discernible although this boundary coincides with the background layer boundary, as shown in Fig. 8(b), (e), (h), and (k). On the other hand, the homogeneous profiles of the rotation angles of the optical axes of the circular disk and the square are also well reconstructed although they straddle different background layers, as shown in Fig. 8(n). When 20-dB noise is added to the scattered field data, as shown in the third column of Fig. 8, the two homogeneous parts in the reconstructed permittivity and conductivity profiles still can be observed although their boundaries are severely distorted. The rough circular and square shapes in the reconstructed

rotation angle profile shown in Fig. 8(o) are also observed. These results indicate that our FEBI-LM solver also has the antinoise ability for the reconstruction of multiple anisotropic scatterers straddling multiple planar layers.

Fig. 9(a) shows the data misfit variations of the FEBI-LM iterations for both the noise-free and noisy cases. Obviously, the data misfit value can reach as low as 0.2% after 268 iteration steps when it is noise-free. By contrast, it only oscillates around the 10% level when 20-dB noise is added. Note the iterations are terminated when no "background" elements can be further removed by SCC. The strong oscillation of the data-misfit curve for the noise-free case is due to the fact that the SCC obligatorily removes some "background" pixels which leads to the local fluctuation of the original curve without SCC applied. Fig. 9(b)–(f) shows the model misfit variations of five anisotropic parameters in corresponding iteration steps. We can see they have similar trends at the beginning of iterations. However, the model misfits for the noise-free cases can reach a much lower level compared with those for the noisy case when iterations terminate. Meanwhile, the final model misfits of permittivity are smaller than those of conductivity when the iteration terminates. Such a phenomenon is also observed in the reconstruction of isotropic profiles shown in Fig. 6. In addition, the final model misfits of the reconstructed rotation angles are also larger than those of permittivity and conductivity, which is also observed in our previous work [41] for the reconstruction of anisotropic scatterers placed in a homogeneous background medium. This is mainly caused by the complicated sensitivity formulation of the scattered fields with respect to the rotation angles. The detailed explanation has been given in [41]. Another noticeable phenomenon is that the model-misfit curves of the conductivity show obvious upturned tails when 20-dB noise is added while those of the permittivity have no such trend. This is because the measured scattered fields are less sensitive to conductivity than to permittivity at the operation frequency of 300 MHz. The magnitude of the noise superposed to the measured scattered field data may be larger than the contribution from the conductivity, which leads to the observed instability.

VI. CONCLUSION AND SUMMARY

In this work, we developed an FWI scheme based on the hybrid FEBI forward solver to reconstruct both the 2-D isotropic scatterers placed across several isotropic planar layers and the 2-D arbitrarily anisotropic scatterers placed across several biaxially anisotropic planar layers. In order to efficiently perform the forward scattering computation, we use a smooth 1-D boundary straddling several background layers to enclose the 2-D inhomogeneous regions within which the scatterers are placed. Both the 2-D Helmholtz equation used to formulate the EM fields inside the enclosed region and the 1-D IE with the aid of layered-medium DGFs used to formulate EM fields along the 1-D boundary are discretized and combined to form the hybrid system matrix. In the FWI, the sensitivity matrix is assembled via taking the first-order derivative of the mass-matrix part of the whole system matrix used in the forward scattering to the isotropic model parameters in the TE mode but taking the first-order derivative of the

stiffness-matrix part to multiple anisotropic model parameters in the TM mode. The LM is adopted to reconstruct both the isotropic and anisotropic dielectric parameters.

Several numerical experiments are performed to prove the correctness and computation efficiency of the proposed FEBI-LM method for scattering and inverse scattering of both isotropic and anisotropic objects straddling multiple subsurface planar layers. It is found that, compared to the traditional FEM with PMLs, the hybrid FEBI method can achieve the same computation accuracy but with much less time and significantly lower memory cost for representative EM scattering configurations. In the FWI, numerical results show that the LM method is able to reconstruct not only the isotropic parameters but also the anisotropic parameters including the optical axis rotation angle even when the measured scattered field data are contaminated by 20-dB noise. Although the field-measured data are temporarily unavailable to validate our proposed methods, they provide a feasible and efficient solution for EM scattering and inverse scattering of 2-D objects straddling multiple subsurface planar layers which are always encountered in practical engineering application scenarios such as soil water monitoring [9], [20], landmine detection [8], [24], and complex geophysical exploration [32].

APPENDIX A

It is assumed both the EM fields and the planarly layered background medium are invariant along the $\hat{y}$-direction in the 2-D problem. The layer interfaces are perpendicular to the $\hat{z}$-axis. The 2-D source point locates at $\boldsymbol{\rho}' = \hat{x}x' + \hat{z}z'$ while the 2-D field point locates at $\boldsymbol{\rho} = \hat{x}x + \hat{z}z$. The source-point layer has the relative permittivity $\overline{\overline{\epsilon}}'_b = \hat{x}\hat{x}\epsilon'_x + \hat{z}\hat{z}\epsilon'_z$ while the field-point layer has the relative permittivity $\overline{\overline{\epsilon}}_b = \hat{x}\hat{x}\epsilon_x + \hat{z}\hat{z}\epsilon_z$. For the TM mode, we have $\mathbf{E} = \hat{x}E_x + \hat{z}E_z$, $\mathbf{H} = \hat{y}H_y$, $\mathbf{J} = \hat{x}J_x + \hat{z}J_z$, and $\mathbf{M} = \hat{y}M_y$. According to the transmission-line analogy method presented in [45], each component of the 2-D TM-mode layered-medium DGFs can be evaluated via the 1-D inverse Fourier transform

$$G_{EJ}^{xx}(\boldsymbol{\rho}, \boldsymbol{\rho}') = \frac{1}{2\pi} \int_{-\infty}^{+\infty} -V_i^e(k_x, z, z') e^{-jk_x(x-x')} dk_x \quad \text{(A1a)}$$

$$G_{EJ}^{zx}(\boldsymbol{\rho}, \boldsymbol{\rho}') = \frac{1}{2\pi} \int_{-\infty}^{+\infty} \frac{k_x}{\omega \varepsilon_0 \epsilon_z} I_i^e(k_x, z, z') e^{-jk_x(x-x')} dk_x$$
$$\text{(A1b)}$$

$$G_{EJ}^{xz}(\boldsymbol{\rho}, \boldsymbol{\rho}') = \frac{1}{2\pi} \int_{-\infty}^{+\infty} \frac{k_x}{\omega \varepsilon_0 \epsilon'_z} V_v^e(k_x, z, z') e^{-jk_x(x-x')} dk_x$$
$$\text{(A1c)}$$

$$G_{EJ}^{zz}(\boldsymbol{\rho}, \boldsymbol{\rho}') = \frac{1}{2\pi} \int_{-\infty}^{+\infty} \frac{-k_x^2}{\omega^2 \varepsilon_0^2 \epsilon_z \epsilon'_z} I_v^e(k_x, z, z') e^{-jk_x(x-x')} dk_x$$
$$\text{(A1d)}$$

$$G_{HJ}^{yx}(\boldsymbol{\rho}, \boldsymbol{\rho}') = \frac{1}{2\pi} \int_{-\infty}^{+\infty} -I_i^e(k_x, z, z') e^{-jk_x(x-x')} dk_x \quad \text{(A1e)}$$

$$G_{HJ}^{yz}(\boldsymbol{\rho}, \boldsymbol{\rho}') = \frac{1}{2\pi} \int_{-\infty}^{+\infty} \frac{k_x}{\omega \varepsilon_0 \epsilon'_z} I_v^e(k_x, z, z') e^{-jk_x(x-x')} dk_x$$
$$\text{(A1f)}$$

$$G_{EM}^{xy}(\boldsymbol{\rho}, \boldsymbol{\rho}') = \frac{1}{2\pi} \int_{-\infty}^{+\infty} -V_v^e(k_x, z, z') e^{-jk_x(x-x')} dk_x \quad \text{(A1g)}$$

$$G_{EM}^{zy}(\boldsymbol{\rho}, \boldsymbol{\rho}') = \frac{1}{2\pi} \int_{-\infty}^{+\infty} \frac{k_x}{\omega \varepsilon_0 \epsilon_z} I_v^e(k_x, z, z') e^{-jk_x(x-x')} dk_x$$
$$\text{(A1h)}$$

$$G_{HM}^{yy}(\boldsymbol{\rho}, \boldsymbol{\rho}') = \frac{1}{2\pi} \int_{-\infty}^{+\infty} -I_v^e(k_x, z, z') e^{-jk_x(x-x')} dk_x \quad \text{(A1i)}$$

where the specific expressions of the voltage terms V_i^e and V_v^e and the current terms I_i^e and I_v^e can be found in [46]. Note the integration may converge slowly when the source point and the field point are close in the vertical $\hat{z}$-direction. In this situation, the primary-field parts of DGFs can be evaluated using the analytical expressions given in [47, Appendix B]. In addition, the 2-D DGFs for the TE mode can be directly evaluated based on (A1) according to the duality theorem.

APPENDIX B

For the 2-D FEM, the basis functions are directly defined in the reference $\xi\eta$ domain with $\xi \in [-1\ 1]$ and $\eta \in [-1\ 1]$ [48]. Any variable ϕ in a square reference element can be expanded by

$$\phi(\xi, \eta) = \sum_{j=1}^{4} c_j \phi_j(\xi, \eta) \quad \text{(B1)}$$

where $c_{j=1,\dots,4}$ are four coefficients in four vertexes of the square element which are arranged anticlockwise, and $\phi_{j=1,\dots,4}$ are four corresponding bilinear Lagrange polynomials which are defined as

$$\phi_1(\xi, \eta) = \frac{1}{4}(1 - \xi)(1 - \eta) \quad \text{(B2a)}$$

$$\phi_2(\xi, \eta) = \frac{1}{4}(1 + \xi)(1 - \eta) \quad \text{(B2b)}$$

$$\phi_3(\xi, \eta) = \frac{1}{4}(1 + \xi)(1 + \eta) \quad \text{(B2c)}$$

$$\phi_4(\xi, \eta) = \frac{1}{4}(1 - \xi)(1 + \eta). \quad \text{(B2d)}$$

REFERENCES

[1] X. Chen, *Computational Methods for Electromagnetic Inverse Scattering*. Singapore: Wiley, 2018.

[2] R. Hong et al., "3-D MRI-based electrical properties tomography using the volume integral equation method," *IEEE Trans. Microw. Theory Techn.*, vol. 65, no. 12, pp. 4802–4811, Dec. 2017.

[3] F. García-Rial, D. Montesano, I. Gómez, C. Callejero, F. Bazus, and J. Grajal, "Combining commercially available active and passive sensors into a millimeter-wave imager for concealed weapon detection," *IEEE Trans. Microw. Theory Techn.*, vol. 67, no. 3, pp. 1167–1183, Mar. 2019.

[4] T. Jun Cui, W. Cho Chew, A. A. Aydiner, and S. Chen, "Inverse scattering of two-dimensional dielectric objects buried in a lossy earth using the distorted Born iterative method," *IEEE Trans. Geosci. Remote Sens.*, vol. 39, no. 2, pp. 339–346, Feb. 2001.

[5] T. R. Madden and R. L. Mackie, "Three-dimensional magnetotelluric modelling and inversion," *Proc. IEEE*, vol. 77, no. 2, pp. 318–333, Feb. 1989.

[6] S. Busch, J. van der Kruk, J. Bikowski, and H. Vereecken, "Quantitative conductivity and permittivity estimation using full-waveform inversion of on-ground GPR data," *Geophysics*, vol. 77, no. 6, pp. H79–H91, Nov. 2012.

[7] K. Yee, "Numerical solution of initial boundary value problems involving Maxwell's equations in isotropic media," *IEEE Trans. Antennas Propag.*, vol. AP-14, no. 3, pp. 302–307, May 1966.

[8] I. Giannakis, A. Giannopoulos, and C. Warren, "A realistic FDTD numerical modeling framework of ground penetrating radar for landmine detection," *IEEE J. Sel. Topics Appl. Earth Observ. Remote Sens.*, vol. 9, no. 1, pp. 37–51, Jan. 2016.

[9] J. S. Buchner, U. Wollschläger, and K. Roth, "Inverting surface GPR data using FDTD simulation and automatic detection of reflections to estimate subsurface water content and geometry," *Geophysics*, vol. 77, no. 4, pp. H45–H55, Jul. 2012.

[10] M. Commer and G. Newman, "A parallel finite-difference approach for 3D transient electromagnetic modeling with galvanic sources," *Geophysics*, vol. 69, no. 5, pp. 1192–1202, Sep. 2004.

[11] S. de la Kethulle de Ryhove and R. Mittet, "3D marine magnetotelluric modeling and inversion with the finite-difference time-domain method," *Geophysics*, vol. 79, no. 6, pp. E269–E286, Nov. 2014.

[12] N. Han, M. J. Nam, H. J. Kim, T. J. Lee, Y. Song, and J. H. Suh, "Efficient three-dimensional inversion of magnetotelluric data using approximate sensitivities," *Geophys. J. Int.*, vol. 175, no. 2, pp. 477–485, Nov. 2008.

[13] R. Streich, "3D finite-difference frequency-domain modeling of controlled-source electromagnetic data: Direct solution and optimization for high accuracy," *Geophysics*, vol. 74, no. 5, pp. F95–F105, Sep. 2009.

[14] Z. Wu, Y. Fan, J. Wang, R. Zhang, and Q. H. Liu, "Application of 2.5-D finite difference method in logging-while-drilling electromagnetic measurements for complex scenarios," *IEEE Geosci. Remote Sens. Lett.*, vol. 17, no. 4, pp. 577–581, Apr. 2020.

[15] Z. Long, H. Cai, X. Hu, G. Li, and O. Shao, "Parallelized 3-D CSEM inversion with secondary field formulation and hexahedral mesh," *IEEE Trans. Geosci. Remote Sens.*, vol. 58, no. 10, pp. 6812–6822, Oct. 2020.

[16] J. Xie et al., "3-D magnetotelluric inversion and application using the edge-based finite element with hexahedral mesh," *IEEE Trans. Geosci. Remote Sens.*, vol. 60, 2022, Art. no. 4503011.

[17] Y. Zhou, L. Shi, N. Liu, C. Zhu, Y. Sun, and Q. H. Liu, "Mixed spectral-element method for overcoming the low-frequency breakdown problem in subsurface EM exploration," *IEEE Trans. Geosci. Remote Sens.*, vol. 55, no. 6, pp. 3488–3500, Jun. 2017.

[18] X. Han et al., "3D finite-element forward modeling of airborne EM systems in frequency-domain using octree meshes," *IEEE Trans. Geosci. Remote Sens.*, vol. 60, 2022, Art. no. 5912813.

[19] Y. Zhou, M. Zhuang, L. Shi, G. Cai, N. Liu, and Q. H. Liu, "Spectral-element method with divergence-free constraint for 2.5-D marine CSEM hydrocarbon exploration," *IEEE Geosci. Remote Sens. Lett.*, vol. 14, no. 11, pp. 1973–1977, Nov. 2017.

[20] G. Serbin and D. Or, "Ground-penetrating radar measurement of soil water content dynamics using a suspended horn antenna," *IEEE Trans. Geosci. Remote Sens.*, vol. 42, no. 8, pp. 1695–1705, Aug. 2004.

[21] G. K. Avdikos and H. T. Anastassiu, "Computational cost estimations and comparisons for three methods of applied electromagnetics (MoM, MAS, MMAS)," *IEEE Antennas Propag. Mag.*, vol. 47, no. 1, pp. 121–129, Feb. 2005.

[22] P. Zwamborn and P. M. van den Berg, "The three dimensional weak form of the conjugate gradient FFT method for solving scattering problems," *IEEE Trans. Microw. Theory Techn.*, vol. 40, no. 9, pp. 1757–1766, Sep. 1992.

[23] H. Gan and W. C. Chew, "A discrete BCG-FFT algorithm for solving 3D inhomogeneous scatterer problems," *J. Electromagn. Waves Appl.*, vol. 9, no. 10, pp. 1339–1357, Jan. 1995.

[24] X. Min Xu and Q. H. Liu, "The BCGS-FFT method for electromagnetic scattering from inhomogeneous objects in a planarly layered medium," *IEEE Antennas Wireless Propag. Lett.*, vol. 1, pp. 77–80, 2002.

[25] K. Yang and A. E. Yilmaz, "A three-dimensional adaptive integral method for scattering from structures embedded in layered media," *IEEE Trans. Geosci. Remote Sens.*, vol. 50, no. 4, pp. 1130–1139, Apr. 2012.

[26] J. R. Phillips and J. K. White, "A precorrected-FFT method for electrostatic analysis of complicated 3-D structures," *IEEE Trans. Comput.-Aided Design Integr. Circuits Syst.*, vol. 16, no. 10, pp. 1059–1072, Oct. 1997.

[27] Q. Huo Liu, Z. Qing Zhang, and X. Min Xu, "The hybrid extended Born approximation and CG-FFT method for electromagnetic induction problems," *IEEE Trans. Geosci. Remote Sens.*, vol. 39, no. 2, pp. 347–355, Feb. 2001.

[28] J. Li, J. Zhuo, Z. Guan, F. Han, and Q. H. Liu, "3-D electromagnetic scattering and inverse scattering by magnetodielectric objects with arbitrary anisotropy in layered uniaxial media," *IEEE Trans. Antennas Propag.*, vol. 68, no. 2, pp. 1009–1022, Feb. 2020.

[29] Y. Hu, Y. Fang, D. LaBrecque, M. Ahmadian, and Q. H. Liu, "Reconstruction of high-contrast proppant in hydraulic fractures with galvanic measurements," *IEEE Trans. Geosci. Remote Sens.*, vol. 56, no. 4, pp. 2066–2073, Apr. 2018.

[30] Y. Chu et al., "Fast microwave through wall imaging method with inhomogeneous background based on Levenberg–Marquardt algorithm," *IEEE Trans. Microw. Theory Techn.*, vol. 67, no. 3, pp. 1138–1147, Mar. 2019.

[31] J. Wang, J. Li, Y. Chen, F. Han, and Q. H. Liu, "Simulation of 3-D electromagnetic scattering and inverse scattering by arbitrary anisotropic dielectric objects embedded in layered arbitrary anisotropic media," *IEEE Trans. Antennas Propag.*, vol. 68, no. 8, pp. 6473–6478, Aug. 2020.

[32] D. Wang et al., "Fast 3-D volume integral equation domain decomposition method for electromagnetic scattering by complex inhomogeneous objects traversing multiple layers," *IEEE Trans. Antennas Propag.*, vol. 68, no. 2, pp. 958–966, Feb. 2020.

[33] R. Huang, Q. Wu, and F. Han, "3-D EM scattering and inverse scattering by anisotropic objects straddling multiple planar uniaxial layers with a 2-D locally rough surface," *IEEE Trans. Antennas Propag.*, vol. 71, no. 11, pp. 8936–8948, Nov. 2023.

[34] Q. Wu, R. Huang, and F. Han, "2-D EM scattering and inverse scattering from inhomogeneous objects straddling multiple subsurface planar layers with a rough surface," *IEEE Geosci. Remote Sens. Lett.*, vol. 21, pp. 1–5, 2024.

[35] M. A. Morgan, C. H. Chen, S. C. Hill, and P. W. Barber, "Finite element-boundary integral formulation for electromagnetic scattering," *Wave Motion*, vol. 6, no. 1, pp. 91–103, Jan. 1984.

[36] J.-M. Jin and V. V. Liepa, "Application of hybrid finite element method to electromagnetic scattering from coated cylinders," *IEEE Trans. Antennas Propag.*, vol. 36, no. 1, pp. 50–54, Jan. 1988.

[37] X. Yuan, D. R. Lynch, and J. W. Strohbehn, "Coupling of finite element and moment methods for electromagnetic scattering from inhomogeneous objects," *IEEE Trans. Antennas Propag.*, vol. 38, no. 3, pp. 386–393, Mar. 1990.

[38] X. Yuan, "Three-dimensional electromagnetic scattering from inhomogeneous objects by the hybrid moment and finite element method," *IEEE Trans. Microw. Theory Techn.*, vol. 38, no. 8, pp. 1053–1058, Aug. 1990.

[39] Wikipedia. *Levenberg–Marquardt Algorithm*. Accessed: Jan. 5, 2024. [Online]. Available: https://en.wikipedia.org/wiki/Levenberg-Marquardt_algorithm

[40] J. Li, Z. Guan, J. Wang, L.-Y. Xiao, and Q. H. Liu, "Contracting electromagnetic full-wave inversion of 2-D inhomogeneous objects with irregular shapes based on the hybrid SESI forward solver," *IEEE Trans. Geosci. Remote Sens.*, vol. 60, 2022, Art. no. 5305411.

[41] J. Li, Z. Li, Z. Guan, and F. Han, "2-D electromagnetic scattering and inverse scattering from anisotropic objects under TE illumination solved by the hybrid SIM/SEM," *IEEE Trans. Antennas Propag.*, vol. 72, no. 4, pp. 3517–3528, Apr. 2024.

[42] K. Agarwal, L. Pan, and X. Chen, "Subspace-based optimization method for reconstruction of 2-D complex anisotropic dielectric objects," *IEEE Trans. Microw. Theory Techn.*, vol. 58, no. 4, pp. 1065–1074, Apr. 2010.

[43] M. Cui, Y. Zhao, B. Xu, and X.-W. Gao, "A new approach for determining damping factors in Levenberg–Marquardt algorithm for solving an inverse heat conduction problem," *Int. J. Heat Mass Transf.*, vol. 107, pp. 747–754, Apr. 2017.

[44] J. Zhuo, L. Ye, F. Han, L. Xiong, and Q. H. Liu, "Multiparametric electromagnetic inversion of 3-D biaxial anisotropic objects embedded in layered uniaxial media using VBIM enhanced by structural consistency constraint," *IEEE Trans. Antennas Propag.*, vol. 68, no. 6, pp. 4774–4785, Jun. 2020.

[45] K. A. Michalski and J. R. Mosig, "Multilayered media Green's functions in integral equation formulations," *IEEE Trans. Antennas Propag.*, vol. 45, no. 3, pp. 508–519, Mar. 1997.

[46] F. Han, J. Zhuo, S. Lu, J. Wang, and Q. H. Liu, "Explicit semianalytical expressions of sensitivity matrices for the reconstruction of 1-D planarly layered TI media illuminated by 3-D sources," *IEEE Trans. Antennas Propag.*, vol. 70, no. 2, pp. 1547–1552, Feb. 2022.

[47] Z. Guan, J. Li, and F. Han, "Exponential accuracy solutions of 2-D electromagnetic scattering from multilayered nonconcentric elliptical magnetodielectric cylinders under TE illumination," *IEEE Trans. Microw. Theory Techn.*, vol. 72, no. 5, pp. 2914–2926, May 2024.

[48] O. Ozgun and M. Kuzuoğlu, *MATLAB-Based Finite Element Programming in Electromagnetic Modeling*. Boca Raton, FL, USA: CRC Press, 2019, ch. 5.